nature physics

ARTICLES

PUBLISHED ONLINE: 13 JULY 2014 | DOI: 10.1038/NPHYS3003

Nanoemulsions obtained via bubble-bursting at a compound interface

Jie Feng[1], Matthieu Roché[1†], Daniele Vigolo[1‡], Luben N. Arnaudov[2], Simeon D. Stoyanov[2,3,4], Theodor D. Gurkov[5], Gichka G. Tsutsumanova[6] and Howard A. Stone[1*]

Bursting of bubbles at an air/liquid interface is a familiar occurrence relevant to foam stability, cell cultures in bioreactors and ocean–atmosphere mass transfer. In the latter case, bubble-bursting leads to the dispersal of sea-water aerosols in the surrounding air. Here we show that bubbles bursting at a compound air/oil/water-with-surfactant interface can disperse submicrometre oil droplets in water. Dispersal results from the detachment of an oil spray from the bottom of the bubble towards water during bubble collapse. We provide evidence that droplet size is selected by physicochemical interactions between oil molecules and the surfactants rather than by hydrodynamics. We demonstrate the unrecognized role that this dispersal mechanism may play in the fate of the sea surface microlayer and of pollutant spills by dispersing petroleum in the water column. Finally, our system provides an energy-efficient route, with potential upscalability, for applications in drug delivery, food production and materials science.

In nature, bubbles can be formed easily by multiple processes, such as wave breaking, the impact of raindrops and even changes of the solubility of air in water due to weather and seasons[1]. When a bubble reaches an air/liquid interface, the drainage and rupture of the liquid film that forms the bubble cap finally lead to bubble-bursting, which can mediate a wide range of physical, biological and geological phenomena at the interface and has received significant attention. For instance, the thinning dynamics of the liquid film are important to theories on foam evolution[2], and the high shear stress induced by film retraction during bubble-bursting is the main cause for cell death when sparging is used to increase the oxygen transfer rate in bioreactors[3]. In addition, bubble-bursting also plays a key role in the mass flux between the sea surface and the atmosphere as a source of aerosol droplets in air[4,5]. In such a scenario, previous studies of bubbles bursting at an air/water interface investigated how the dynamics lead to mass transfer from the lower liquid phase to the upper gas phase: aerosols are dispersed into the atmosphere owing to both the disintegration of the top cap of the bubble and the fragmentation of the upwardly directed liquid jet formed at the end of bubble collapse[6–8]. Such mass transfer from the lower to the upper phase also occurs when a rising bubble passes through an oil/water interface: water droplets are dispersed into the upper oil phase because of the rupture of the water film[9].

Here, we describe the reverse transport process, where submicrometre oil droplets, formed during bubble-bursting at a compound interface, are transported from the upper to the lower phase. We are not aware of any previous documentation of this phenomenon. After continuous bubble-bursting at an air/hexadecane/water-with-surfactant interface for dozens of hours (Fig. 1a), the aqueous phase became translucent, which suggested that small objects with a refractive index different from that of water had been dispersed in the lower water phase (Fig. 1b). The analysis of samples of the solution using dynamic light scattering (DLS) confirmed the presence of objects with a radius $r \approx 100$ nm and a moderate polydispersity index (PDI, Supplementary Information; Fig. 1c). As the surfactant concentration in the water phase is well below the critical micelle concentration[10] and we only observe submicrometre objects when there is bubble-bursting, these objects are oil droplets rather than spontaneously generated micro-emulsion droplets or surfactant mesophases. Control experiments confirm that these submicrometre-sized droplets exist only when surfactants are present in the water phase. Measurements of the size of hexadecane droplets on longer timescales showed that r remained constant for at least a week (Fig. 1d). Thus, our experiments demonstrate that the bursting of bubbles at a compound interface can drive mass transport into the bulk liquid to form stable submicrometre droplets.

High-speed visualization of the bubble-bursting process from above the air/oil interface and below the oil/water interface allowed us to understand how oil droplets are dispersed in the surfactant solution. The bubble cap, initially formed of an oil film sitting on a water film, bursts in two steps in most cases (Fig. 2a and Supplementary Movie 1). The experimental images suggest that the top oil film ruptures and retracts first and then the water film breaks. Only the latter step induces droplet production through fragmentation of the receding water film, thus ruling out atomization of the bubble cap as the origin of the submicrometre-sized oil droplets in the aqueous phase. A side view of the bursting bubble below the oil/water interface reveals that oil droplets are dispersed from the bottom of the bubble into the bulk water

---

[1] Department of Mechanical and Aerospace Engineering, Princeton University, Princeton, New Jersey 08544, USA, [2] Unilever Research and Development, 3133AT Vlaardingen, The Netherlands, [3] Laboratory of Physical Chemistry and Colloid Science, Wageningen University, 6703 HB Wageningen, The Netherlands, [4] Department of Mechanical Engineering, University College London, Torrington Place, London WC1E 7JE, UK, [5] Department of Chemical Engineering, Faculty of Chemistry and Pharmacy, Sofia University, Sofia 1164, Bulgaria, [6] Department of Solid State Physics and Microelectronics, Faculty of Physics, Sofia University, Sofia 1164, Bulgaria. †Present address: Laboratoire de Physique des Solides, Université Paris Sud-CNRS, 91405 Orsay, France. ‡Present address: Department of Chemistry and Applied Biosciences, Institute for Chemical and Bioengineering, ETH Zurich, 8093 Zurich, Switzerland. *e-mail: hastone@princeton.edu

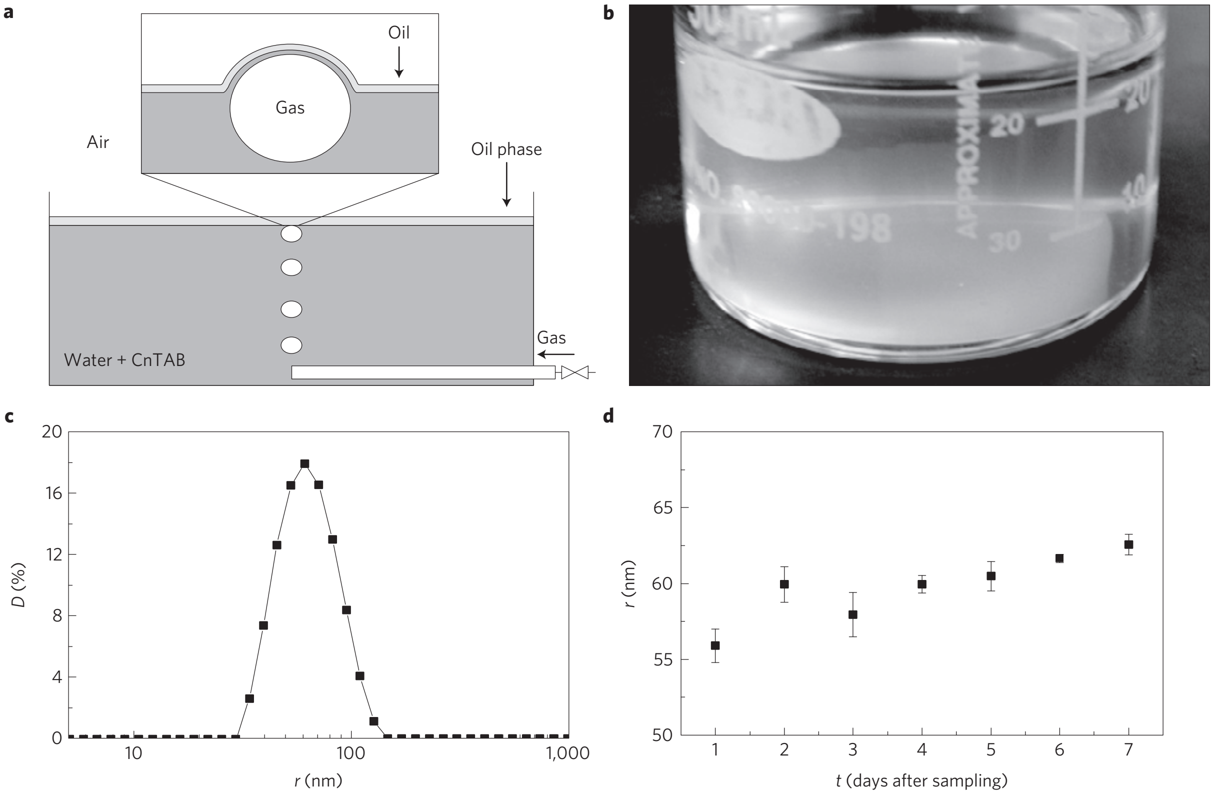

Figure 1 | Bubble-bursting at an air/oil/water interface. a, Sketch of the experimental system. Inset: close-up of the deformed compound interface. **b**, Image of the translucent aqueous phase after bubbling for 48 hours (oil phase: dodecane, aqueous phase: $[\mathrm{C_{16}TAB}] = 0.09$ mM). **c**, Size distribution of the oil droplets based on the intensity measured by dynamic light scattering (DLS) (oil phase: hexadecane, initial thickness of the oil layer $h_l = 1$ mm; bubble diameter $d_b = 2.8 \pm 0.25$ mm, aqueous phase: $[\mathrm{C_{16}TAB}] = 0.09$ mM). The peak value of the distribution (59.8 nm here, with PDI = 0.091) is taken as the radius (r) of the submicrometre droplets. D on the vertical axis represents the distribution of scattering intensity obtained by DLS. **d**, Time evolution of the size of the submicrometre droplets in the same sample shown in Fig. 1c over a week, demonstrating their stability. The error bars here are defined as the standard deviation of the droplet size in three DLS measurements for all subfigures.

(Supplementary Movie 2). We have observed that after a hole opens in the water film (white circle in Fig. 2b1) the surface of the cavity deforms during film retraction (Fig. 2b2 and b3) and a spray of droplets is ejected from the cavity boundary towards the bulk water, at a location opposite to that of the nucleation site of the hole (white circle in Fig. 2b4). Also, we observed that the larger non-Brownian droplets rose rapidly back to the oil/water interface, whereas the smaller objects were ejected deep in the bulk water (Supplementary Movie 3). We speculate that submicrometre-sized droplets are formed and dispersed during this spraying process, although we cannot observe them directly with optical methods.

During the time that we observe droplet formation, the flow close to the bubble–water interface resembles the boundary-layer detachment flow theoretically predicted for the case of a bubble bursting at an air/water interface[11]. The flow around a curved bubble-free interface with a zero-tangential-stress condition generates vorticity from the interface (the fluid elements tend to rotate as they translate). The vorticity is confined to a narrow region adjacent to the air–water boundary, which is referred to as a viscous boundary layer, where both inertial and viscous forces are important. Consequently, when a bubble bursts in our experiment, the wall of the cavity collapses inwards and the fluid converges, the pressure rises in the region beneath the bubble, creating an adverse pressure gradient along the flow direction around the cavity[11] (as schematically shown by $\partial p/\partial x > 0$ in Fig. 2c4). This variation of pressure means that fluid flow tangent to the bubble is slowed and, consequently, there is separation of the boundary layer—that is, streamlines detach nearly perpendicular to the bubble boundary in the neighbourhood of a surface stagnation point. Therefore, there is flow directed away from the interface after bubble bursting, which in our case leads to the spray into the bulk liquid. We performed further model experiments that show that 10-μm latex particles initially sitting on the flat air/water interface without the oil phase are also dispersed from the side of the cavity into the bulk water during bubble-bursting in a fashion similar to the oil droplets (Supplementary Movie 4). Thus, we propose the dispersal mechanism summarized in Fig. 2c. For a bubble at the compound interface, the upper oil film ruptures first, leaving a water film that retracts rapidly after a hole nucleates on the bubble cap (Fig. 2c1–c3). Then, a spray of polydisperse droplets is generated, following the direction of the boundary-layer separation flow from the cavity wall into the bulk (Fig. 2c4).

The similarity of the dispersal mechanism to the predicted boundary-layer detachment flow motivated us to investigate how hydrodynamics may set the size of submicrometre droplets. However, a study of this relationship with more than ten non-aqueous phases and three surfactants in the aqueous phase (Methods) shows that the results are different from most fragmentation processes[12,13]. In particular, because the size of the droplets r we measured is independent of the initial thickness of the oil layer h_l or the bubble diameter d_b (Fig. 3a,b), we used dimensional analysis to determine a characteristic length scale for our system, which depends on viscosity of the oil phase η_o, viscosity of the aqueous phase η_w, density of the oil phase $\rho_o (\approx \rho_w)$ and the interfacial tension between the oil and water γ_{ow}. As $\eta_o \geq \eta_w$, we assume that only η_o is significant, and we obtain $r \sim \eta_o^2/(\rho_o \gamma_{ow})$. However, this naive scaling law fails to capture the three- to five-fold decrease of r with a three-fold increase of η_o (Fig. 3c). In addition,

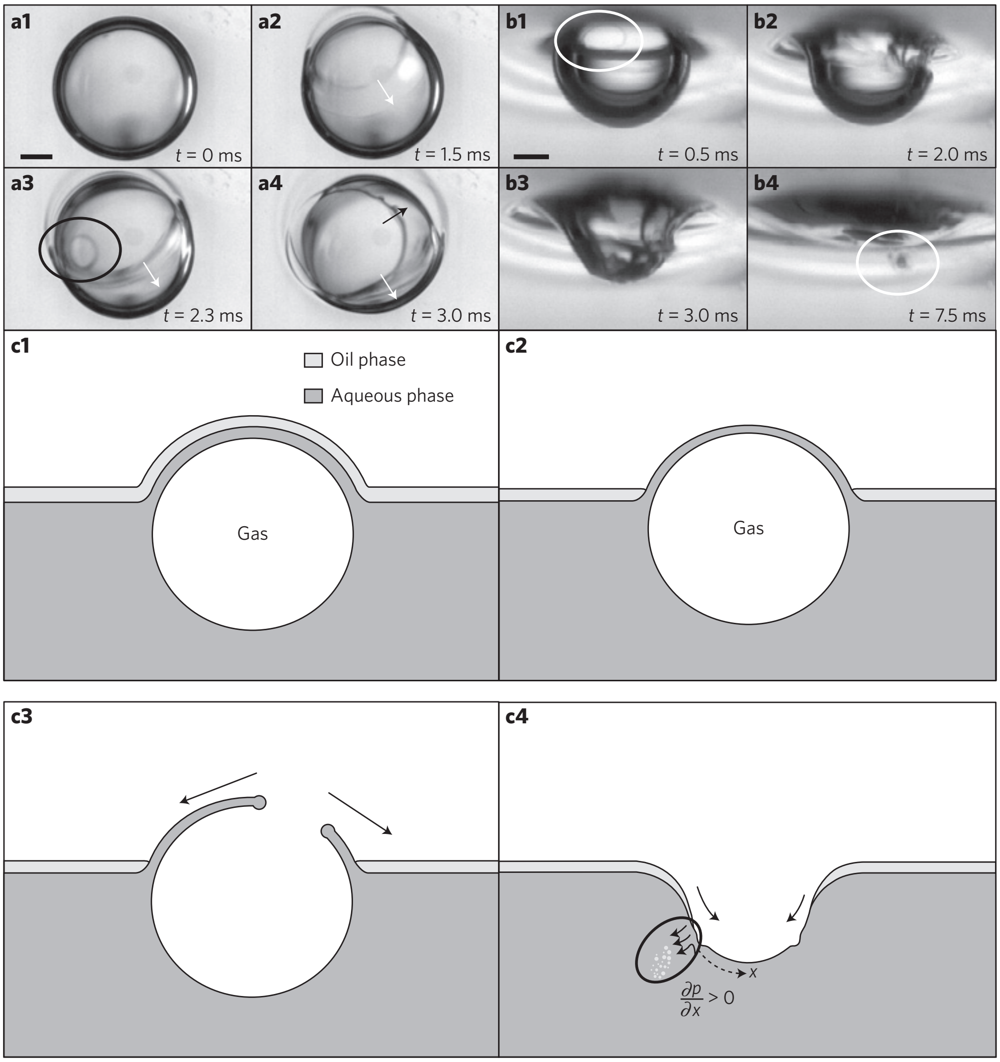

Figure 2 | High-speed observations of the bursting process and schematic descriptions for the dispersal mechanism. **a**, Top-view photos of the bursting of a bubble at interfaces of air/hexadecane/water at $[\mathrm{C_{16}TAB}] = 0.09\,\mathrm{mM}$ ($h_l = 1\,\mathrm{mm}$; $d_b = 4.0 \pm 0.21\,\mathrm{mm}$; scale bar is 1 mm). **a1**, The bubble rests near the compound interface with oil and water films on top of the bubble. **a2**, The oil film (above the water film) ruptures first. The retraction direction of the oil film is indicated by the white arrow. **a3**, After rupture of the oil film, a hole opens in the water film, as shown by the black oval. **a4**, The water film then retracts along a direction different from that of the oil film (shown by the black arrow). **b**, Side-view photos of the bursting of a bubble at interfaces of air/hexadecane/water at $[\mathrm{C_{16}TAB}] = 0.09\,\mathrm{mM}$ ($h_l = 1\,\mathrm{mm}$; $d_b = 4.0 \pm 0.21\,\mathrm{mm}$; scale bar is 1 mm). **b1**, A hole is nucleated on the cap of the bubble, as shown by the white oval. **b2**, The surface of the cavity deforms. **b3**, The deformation propagates further down the interface. **b4**, A spray of droplets is created at the wall of the cavity, as shown by the white oval. Note that the photos in **a** and **b** are not taken simultaneously. **c**, Sketch of the mechanism for the dispersal formation. The flow direction of the boundary-layer detachment is indicated with the arrows in the black oval in **c4**. The adverse pressure gradient $\partial p/\partial x > 0$ is shown schematically.

we observed that r increases with an increase of the speed of the last receding film U_r (Fig. 3d), in contradiction with the expectation that an increase of the energy injected in a two-phase liquid system generates smaller droplets[13,14]. Thus, the size of the submicrometre droplets is independent of hydrodynamics.

We hypothesize that the submicrometre droplet size is set by molecular-scale physicochemical interactions between the oil molecules and the surfactants. At the macroscopic scale, these interactions translate into transitions between three possible wetting states for oil on an aqueous surfactant solution depending on surfactant concentration: partial, pseudo-partial and complete wetting[15–17] (Fig. 4a). We found that dispersal of submicrometre-sized droplets never occurred for liquid combinations showing only a pseudo-partial-to-complete wetting transition (for example, poly(dimethylsiloxane) on aqueous surfactant solutions[18]) or partial wetting for all surfactant concentrations (for example, alkanes on aqueous solutions of Aerosol OT; ref. 15). In contrast, dispersal occurred in systems where only a surfactant-induced transition from partial to pseudo-partial wetting happened. We observed the presence of oil droplets either when the equilibrium surfactant concentration in water was high enough to induce a pseudo-partial wetting state at rest, or when the equilibrium surfactant concentration was smaller than the transition concentration, but sufficiently close to it, so that surfactant compression[19] during bubble-bursting dynamics could trigger a wetting transition.

The correlation between the oil/water wetting state and the occurrence of dispersal also suggests a possible explanation for the origin of the droplets. Pseudo-partial wetting is characterized by the coexistence of oil lenses at equilibrium with a thin film of oil whose thickness is of the order of several molecular sizes[15]. These lenses could be the seeds of our submicrometre droplets. To test this idea, we performed ellipsometry measurements after the deposition of a

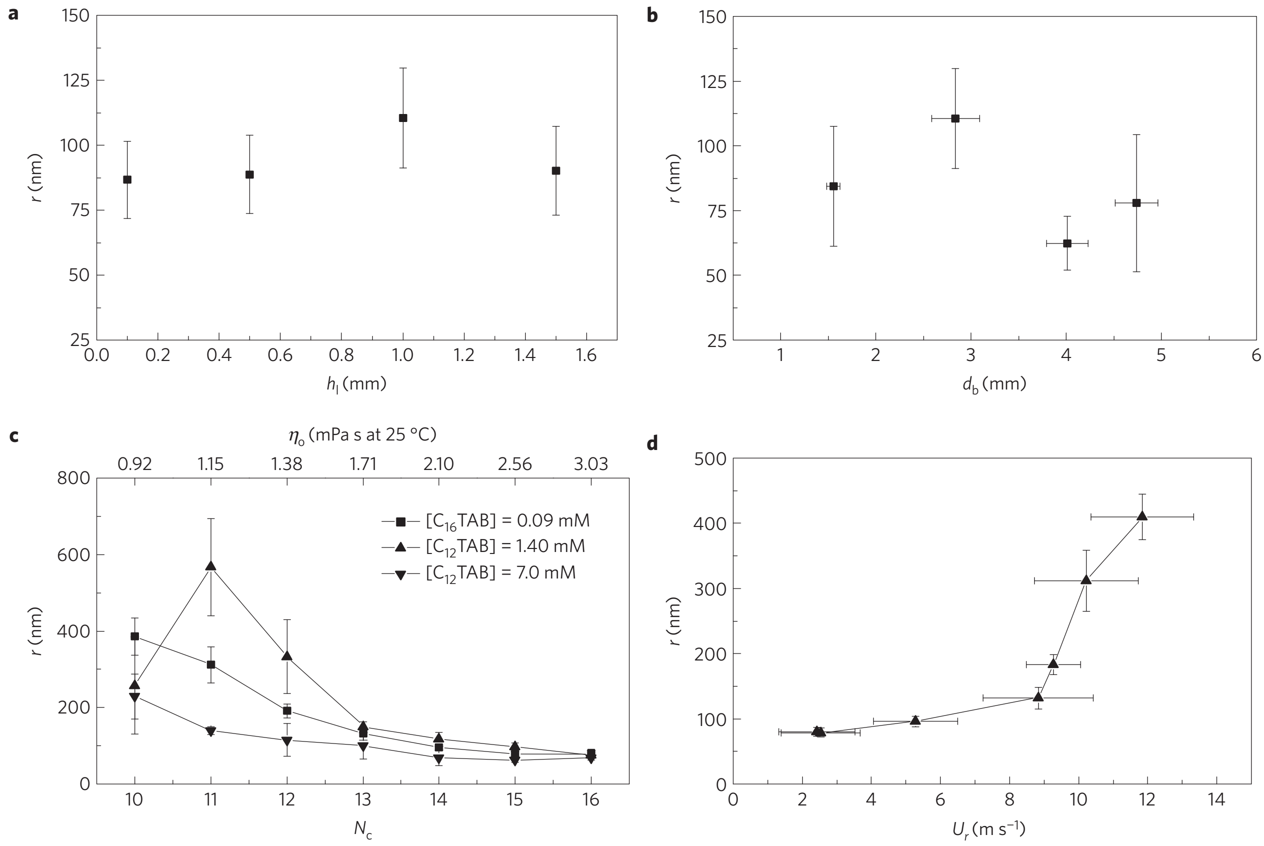

Figure 3 | Influence of oil layer thickness (h_l), bubble diameter (d_b), viscosity of oil (η_o) and carbon number of the oil (N_c) on the radius (r) of the submicrometre-sized droplets. a, Relationship between r and h_l (oil phase: hexadecane; $d_b = 2.8 \pm 0.25$ mm; aqueous phase: [C_{16}TAB] $= 0.09$ mM). **b**, Relationship between r and d_b (oil phase: hexadecane; $h_l = 1$ mm; aqueous phase: [C_{16}TAB] $= 0.09$ mM). **c**, Relationship between r and η_o as well as N_c (oil phase: hexadecane; $h_l = 1$ mm; $d_b = 2.8 \pm 0.25$ mm; aqueous phase: [C_{16}TAB] $= 0.09$ mM and [C_{12}TAB] $= 1.40$ mM or 7.0 mM. Note that r for $N_c = 11$ with [C_{12}TAB] $= 1.40$ mM was determined by a microscope using image analysis because DLS results were unreliable. **d**, Relationship between r and the speed of the rim of the last receding film U_r. The error bars are defined as the standard deviation of three measurements.

millimetre-sized hexadecane droplet on a surfactant solution, which show that small patches with a thickness of the order of 100 nm exist at places on the interface (Methods). We believe that similar lenses form during the dispersal process we propose in Fig. 2c. During the last stage of bubble collapse, oil spreads on the inner surface of the bubble and leads to formation of the lenses in pseudo-partial wetting. These lenses may then be entrained in bulk water by the boundary-layer separation flow (Fig. 2c4).

Next, we use this experimental result to deduce the lateral size and hence the volume of the lenses so as to compare with the volume and the radius of the submicrometre-sized droplets. The wetting state of oil/water + surfactant systems results from a competition between short-range interactions described by the initial spreading coefficient $S_i = \gamma_{aw} - \gamma_{oa} - \gamma_{ow}$, where γ_{ij} is the interfacial tension between air (a), water + surfactants (w) and oil (o), and long-range interactions such as van der Waals forces between air and water through the oil film[15,16], which is described by the Hamaker constant A. Here, we consider only the contribution from non-retarded van der Waals interactions to derive the typical order of magnitude, neglecting other kinds of long-range interactions[20]. Pseudo-partial wetting (also sometimes known as frustrated complete wetting[21]) results from the combination of a positive value for S_i, favouring spreading of the oil on the surfactant solution, and a positive value for A, favouring thinning of the oil film by attractive long-range interactions[16]. In this wetting state, an oil film sitting on the surface of the surfactant solution will become unstable and rupture as it thins, leading to a film consisting of a collection of lenses of height h separated by a layer of nanometre thickness ζ (ref. 22; Fig. 4a2). After lens formation, van der Waals attraction in the thin film is comparable to the capillary pressure in the lens. This force balance allows us to estimate the size of the lens, which we approximate by a spherical cap with a flat bottom. The scaling has the form

$$\frac{A}{6\pi\zeta^3} = \frac{2\gamma_{oa}}{R} \qquad (1)$$

where R, the radius of curvature of the lens, is expressed as $(\lambda^2 + h^2)/(2h)$ (see Supplementary Information for the derivation of the geometrical properties of the lens), h is the thickness (of the order of 100 nm) that we take from the ellipsometry measurements and λ is the lateral size of the lens (Fig. 4a2). Then, $\lambda = O(100\ \text{nm})$. The volume of one lens is $V_{lens} = (\pi h/6)(3\lambda^2 + h^2)$ and we expect the droplet volume to satisfy $4/3\pi r^3 = V_{lens}$ if the lens is the precursor of the submicrometre droplets. Using data available in the literature for γ_{oa}, A and ζ, equation (1) predicts that the droplet radius increases with a decrease of the carbon chain length of the alkanes, in agreement with our experimental results. For example, this model yields a droplet radius of 57 nm for hexadecane and 107 nm for decane (Supplementary Table 2). These sizes are of the same order of magnitude as those we have measured in our experiments. Thus, we believe that the scaling we propose describes a plausible physical picture for the formation process of the submicrometre droplets we observe in the experiments.

The results we report here suggest possible environmental consequences related to bubble-bursting in nature. For example, we have verified that petroleum is dispersed in bulk water

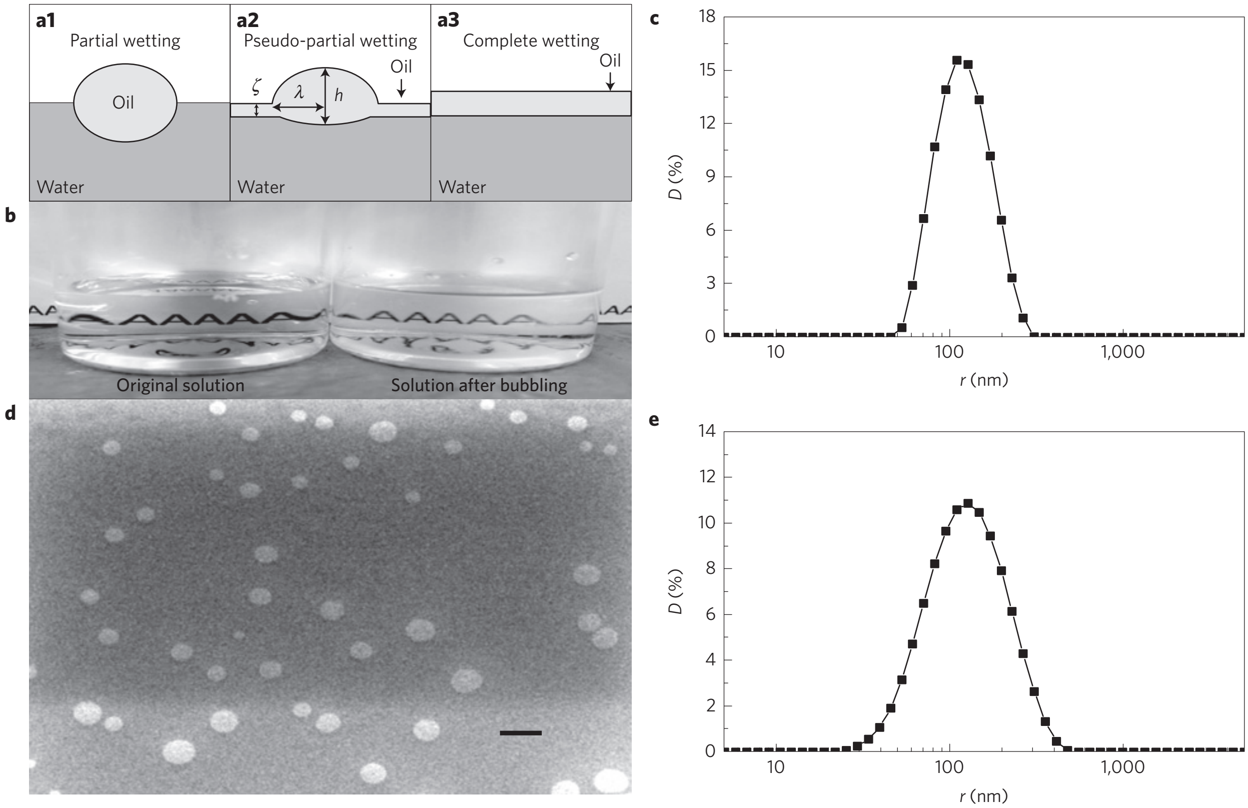

Figure 4 | Sketch of different wetting states and formation of petroleum dispersal and polymeric submicrometre particles. **a**, Partial wetting, pseudo-partial wetting and complete wetting states of an oil drop on an aqueous surface. The partial wetting state is characterized by an oil lens sitting at the air/water interface in equilibrium with a two-dimensional dilute gas of oil molecules, whereas, in the pseudo-partial wetting state, the oil initially spreads after deposition and then forms lenses in equilibrium with a microscopic film a few molecules in thickness. The oil spreads out to form a film of uniform thickness covering the whole surface in the complete wetting state. The variables characterizing the lens dimensions in **a2** are defined in equation (1) and the associated text. **b**, Image of the aqueous phase after bubbling for 48 hours using petroleum as the oil phase ($h_l = 1$ mm; $d_b = 2.8 \pm 0.25$ mm; aqueous phase: [C_{16}TAB] $= 0.09$ mM). The solution after bubbling is hazy compared with the original solution. **c**, Results of DLS measurements for samples of the solution after bubbling. The radius (r) of the droplets is 113.4 nm with PDI = 0.101. **d**, Environmental scanning electron microscope image of ultraviolet-cured submicrometre particles produced by bubble-bursting (oil phase: NOA 89; $h_l = 1$ mm; $d_b = 2.8 \pm 0.25$ mm; aqueous phase: [C_{16}TAB] $= 0.09$ mM). Scale bar is 500 nm. **e**, Results of DLS measurements of the NOA 89 sample before the ultraviolet curing process. The size of the particles is 109.8 nm with PDI = 0.197. In **c** and **e**, D on the vertical axis represents the distribution of scattering intensity obtained by DLS.

by bubble-bursting (Fig. 4b,c). When other well-identified mechanisms, such as wave breaking[23], are limited, bubble-bursting could still lead to dispersal of oil into the lower water phase during oil spills. This dispersal may enhance pollution, where small droplets tend to be digested by sea creatures more easily than on the surface, but dispersal can also help bacteria or algae to degrade pollutants faster because of the high surface-to-volume ratio of the droplets. Also, the interface separating the ocean from Earth's atmosphere is always covered by the sea surface microlayer, which is a physicochemically complex organic film containing significant amounts of surface-active materials, including lipids, proteins and hydrocarbons[24,25], as the alkanes we use in our experiments. The sea surface microlayer is structurally and chemically similar to our compound interface, and our work suggests that the sea surface microlayer may not only be transported into the atmosphere within aerosol droplets produced by bursting bubbles[26], but it might be also be dispersed into the bulk of the oceans, thus redistributing organic matter in the ecosystem. We are not aware of any study investigating mass transfer from the surface of the ocean towards its bulk due to bubble-bursting, which has been related so far only to the formation of wind-dispersed aerosols[27].

Inspired by the application of bubbling to the production of colloids[28] and liposomes[29], our study provides a potential scalable route for the production of dispersions of submicrometre particles, which play an important role in multiple material-related fields[30–32]. As an illustration, we have dispersed droplets of an ultraviolet-curable liquid adhesive (Norland Optical Adhesive (NOA) 89) and cross-linked them using ultraviolet light to obtain solid particles with a size comparable to that of the original droplets (Fig. 4d,e and Methods). Our dispersal method meets several requirements important to industrial applications: its energy efficiency is between 1 and 10%, which is at least one order of magnitude greater than the $O(0.1\%)$ efficiency of classical high-shear-rate methods[33] (see Supplementary Information for detailed calculations). Also, bubble-bursting has the potential to be scaled up, by increasing the bubbling frequency for example (Supplementary Information), while keeping costs low and remaining sustainable, in contrast with mechanical top–down methods. Furthermore, our system works when interfacial tensions are of the order of tens of mN m^{-1}; in contrast, micro-emulsions obtained by spontaneous emulsification[34] require that the interfacial tension between compounds be ultralow. Finally, submicrometre particles are often obtained by bottom–up approaches, such as dispersion polymerization[35], that require the dispersed phase to be soluble in the continuous phase. Our top–down approach releases this limitation as the solvent-insoluble liquid phase, oil here, can be directly dispersed in the form of submicrometre droplets in water (the solvent). As demonstrated in Fig. 4d,e, the droplets can then be cured directly using an appropriate method, such as ultraviolet light or other triggers for chemical reactions. In closing, we believe that our finding of the features of bubble-bursting at a compound interface offers new insights into the dynamical processes of complex fluids, with potential environmental consequences and industrial applications.

Methods

Experimental system. The experimental system is shown in Fig. 1a. For each experiment, a thin layer of the dispersed phase, for example, a non-polar oil, was deposited on an aqueous solution containing an ionic surfactant C_nTAB. Air bubbles were formed at the tip of a tube located at the bottom of the tank. The bubbles rose to the interface because of buoyancy. We changed the size of the bubbles by adjusting the injection pressure and the diameter of the tube. The bubbling frequency was adjusted to 0.1–1 Hz and we made sure there were at most a few bubbles at the interface without forming a bubble column. Each experiment ran for 48 h to produce enough submicrometre droplets to be detected. To reduce the influence of dust, the container was made clean before each experiment. During the experiment, we reduced the contamination of the interface and the bulk by covering the tank. We collected samples deep in the bath and far from the interface. Samples were analysed with DLS 8 h after sampling, without any further treatment. We used a high-speed camera to capture the bubble-bursting process and ellipsometry to characterize the oil layer at the interface. The ultraviolet curing experiments were carried out using an ultraviolet oven (IntelliRay 400, Uvitron) at wavelengths of 320–390 nm and an exposure time of 15 s.

Materials. An aqueous surfactant solution was used as the continuous phase. Ultrapure water (resistivity 18.2 MΩ cm, Millipore MilliQ) was used to prepare all solutions. We used C_{16}TAB (hexadecyltrimethylammonium bromide, Sigma-Aldrich, BioXtra, ≥99%), C_{12}TAB (dodecyltrimethylammonium bromide, Sigma-Aldrich, BioXtra, ∼99%), Aerosol OT (docusate sodium, Sigma-Aldrich) and $C_{12}NaSO_4$ (sodium dodecyl sulphate, ACS reagent, ≥99%, Sigma-Aldrich) in the experiments as the water-soluble surfactants. For the oil phase, we used *n*-hexadecane (Sigma-Aldrich, anhydrous, ≥99%, $\rho = 773\,\mathrm{kg\,m^{-3}}$, $\eta = 3.03\,\mathrm{mPa\,s}$ at 25 °C), *n*-pentadecane (Sigma-Aldrich, ≥99%, $\rho = 769\,\mathrm{kg\,m^{-3}}$, $\eta = 2.56\,\mathrm{mPa\,s}$ at 25 °C), *n*-tetradecane (Sigma-Aldrich, olefine free, ≥99%, $\rho = 762\,\mathrm{kg\,m^{-3}}$, $\eta = 2.10\,\mathrm{mPa\,s}$ at 25 °C), *n*-tridecane (Sigma-Aldrich, ≥99%, $\rho = 756\,\mathrm{kg\,m^{-3}}$, $\eta = 1.71\,\mathrm{mPa\,s}$ at 25 °C), *n*-dodecane (Sigma-Aldrich, anhydrous, ≥99%, $\rho = 750\,\mathrm{kg\,m^{-3}}$, $\eta = 1.38\,\mathrm{mPa\,s}$ at 25 °C), *n*-undecane (Sigma-Aldrich, ≥99%, $\rho = 740\,\mathrm{kg\,m^{-3}}$, $\eta = 1.15\,\mathrm{mPa\,s}$ at 25 °C), *n*-decane (Sigma-Aldrich, anhydrous, ≥99%, $\rho = 730\,\mathrm{kg\,m^{-3}}$, $\eta = 0.92\,\mathrm{mPa\,s}$ at 25 °C), and poly(dimethylsiloxane) (Sigma-Aldrich, $\upsilon = 1$, 5 or 10 cSt at 25 °C). The ultraviolet-cured material in Fig. 4d,e is NOA 89 which is cured by ultraviolet light with maximum absorption in the range 310–395 nm.

High-speed imaging. A high-speed camera (Vision Research, Phantom V7.3) with a lens (Sigma, DG Macro 105 mm) was used to record high-speed videos of the bubble collapse, at frame rates from 6,800 up to 32,000 fps. Movies were processed using Fiji software.

Dynamic light scattering. The size of the submicrometre droplets was determined by dynamic light scattering (DLS) using a Malvern Zetasizer Nano ZS. The measurements were performed at scattering angles of 12.8° or 173° with a 4 mW He–Ne laser producing light at a wavelength of 633 nm. DLS data were processed with Malvern's software using a distribution analysis based on a cumulant model to fit a single exponential to the correlation function to obtain the cumulant mean size and size distribution of the submicrometre droplets. The cumulant analysis is defined in ISO standard document 13321. The calculations of the PDI are defined in the ISO standard document 13321:1996 E. Results of the PDI in different measurements are shown in the Supplementary Information.

Ellipsometry. Ellipsometry experiments are carried out in the following way: polarized laser light (with wavelength 532 nm) was shone at the surface of a Petri dish with an aqueous solution of $[C_{16}\mathrm{TAB}] = 0.9$ mM and the reflected signal was recorded with a detector. The set-up is based on a null type ellipsometer (LEF 3M, Novosibirsk, Russia), equipped with a rotating analyzer unit that allows one to measure the changes in reflected light polarization in time steps of ∼0.2 s. The angle of incidence is 50.0°. The instrument records the ellipsometric angles Ψ and Δ, where $\tan\Psi\exp(i\Delta)$ is the polarization ratio of the output to the input signal. The technique is described in detail elsewhere[36]. As the laser spot has finite dimensions (∼1 mm^2), the values of Ψ and Δ are the average ones for the entities present in this spot. When stable base lines at the air/ aqueous C_{16}TAB boundary were established, a drop of 10 µl hexadecane was carefully added on the interface (far from the laser beam) and changes in polarization were detected, which in turn allow the calculation of the film thickness (assuming a refractive index of hexadecane $n = 1.4340$).

Received 21 November 2013; accepted 22 May 2014;

References

1. Blanchard, D. C. & Woodcock, A. H. Bubble formation and modification in the sea and its meteorological significance. *Tellus* **9,** 145–158 (1957).
2. Tong, M., Cole, K. & Neethling, S. J. Drainage and stability of 2D foams: Foam behaviour in vertical Hele–Shaw cells. *Colloids Surf. A* **382,** 42–49 (2011).
3. Moheimani, N. R., Isdepsky, A., Lisec, J., Raes, E. & Borowitzka, M. A. Coccolithophorid algae culture in closed photobioreactors. *Biotechnol. Bioeng.* **108,** 2078–2087 (2011).
4. Wu, J. Evidence of sea spray produced by bursting bubbles. *Science* **212,** 324–326 (1981).
5. Schmitt-Kopplin, P. *et al.* Dissolved organic matter in sea spray: a transfer study from marine surface water to aerosols. *Biogeosciences* **9,** 1571–1582 (2012).
6. Duchemin, L., Popinet, S., Josserand, C. & Zaleski, S. Jet formation in bubbles bursting at a free surface. *Phys. Fluids* **14,** 3000–3008 (2002).
7. Bird, J. C., de Ruiter, R., Courbin, L. & Stone, H. A. Daughter bubble cascades produced by folding of ruptured thin films. *Nature* **465,** 759–762 (2010).
8. Lhuissier, H. & Villermaux, E. Bursting bubble aerosols. *J. Fluid Mech.* **696,** 5–44 (2012).
9. Uemura, T., Ueda, Y. & Iguchi, M. Ripples on a rising bubble through an immiscible two-liquid interface generate numerous micro droplets. *Europhys. Lett.* **92,** 34004 (2010).
10. Mukerjee, P. & Mysels, K. J. *Critical Micelle Concentrations of Aqueous Surfactant Systems* (US National Bureau of Standards; for sale by the Supt of Docs, US Govt Print Off, 1971).
11. Boulton-Stone, J. M. & Blake, J. R. Gas-bubbles bursting at a free surface. *J. Fluid Mech.* **254,** 437–466 (1993).
12. Eggers, J. & Villermaux, E. Physics of liquid jets. *Rep. Prog. Phys.* **71,** 036601 (2008).
13. Walstra, P. Principles of emulsion formation. *Chem. Eng. Sci.* **48,** 333–349 (1993).
14. Marmottant, P. H. & Villermaux, E. On spray formation. *J. Fluid Mech.* **498,** 73–111 (2004).
15. Wilkinson, K. M., Bain, C. D., Matsubara, H. & Aratono, M. Wetting of surfactant solutions by alkanes. *ChemPhysChem* **6,** 547–555 (2005).
16. Ash, P. A., Bain, C. D. & Matsubara, H. Wetting in oil/water/surfactant systems. *Curr. Opin. Colloid Interf.* **17,** 196–204 (2012).
17. Kellay, H., Meunier, J. & Binks, B. P. Wetting properties of normal-alkanes on AOT monolayers at the brine–air interface. *Phys. Rev. Lett.* **69,** 1220–1223 (1992).
18. Cheng, Y., Ye, X., Huang, X. D. & Ma, H. R. Reentrant wetting transition on surfactant solution surfaces. *J. Chem. Phys.* **125,** 164709 (2006).
19. Boulton-Stone, J. M. The effect of surfactant on bursting gas-bubbles. *J. Fluid Mech.* **302,** 231–257 (1995).
20. Israelachvili, J. N. *Intermolecular and Surface Forces* 2nd edn (Academic, 1991).
21. Bertrand, E. *et al.* First-order and critical wetting of alkanes on water. *Phys. Rev. Lett.* **85,** 1282–1285 (2000).
22. Matsubara, H., Aratono, A., Wilkinson, K. M. & Bain, C. D. Lattice model for the wetting transition of alkanes on aqueous surfactant solutions. *Langmuir* **22,** 982–988 (2006).
23. Liu, T. & Peter Sheng, Y. Three dimensional simulation of transport and fate of oil spill under wave induced circulation. *Mar. Pollut. Bull.* **80,** 148–159 (2014).
24. Wurl, O., Wurl, E., Miller, L., Johnson, K. & Vagle, S. Formation and global distribution of sea-surface microlayers. *Biogeosciences* **8,** 121–135 (2011).
25. Cunliffe, M. *et al.* Sea surface microlayers: A unified physicochemical and biological perspective of the air–ocean interface. *Prog. Oceanogr.* **109,** 104–116 (2012).
26. Brock, C. A., Murphy, D. M., Bahreini, R. & Middlebrook, A. M. Formation and growth of organic aerosols downwind of the Deepwater Horizon oil spill. *Geophys. Res. Lett.* **38,** L17805 (2011).
27. Sellegri, K., O'Dowd, C. D., Yoon, Y. J., Jennings, S. G. & de Leeuw, G. Surfactants and submicron sea spray generation. *J. Geophys. Res.* **111,** D22215 (2006).
28. Arnaudov, L. N., Stoyanov, S. D. & Stuart, M. A. C. Colloid fabrication by co-extrusion. *Colloids Surf. A* **323,** 94–98 (2008).
29. Talsma, H., Vansteenbergen, M. J., Borchert, J. C. H. & Crommelin, D. J. A. A novel technique for the one-step preparation of liposomes and nonionic surfactant vesicles without the use of organic solvents. Liposome formation in a continuous gas-stream: The bubble method. *J. Pharm. Sci.* **83,** 276–280 (1994).
30. Wang, L. J., Dong, J. F., Chen, J., Eastoe, J. & Li, X. F. Design and optimization of a new self-nanoemulsifying drug delivery system. *J. Colloid Interface Sci.* **330,** 443–448 (2009).

31. Rao, J. & McClements, D. J. Food-grade microemulsions and nanoemulsions: Role of oil phase composition on formation and stability. *Food Hydrocolloids* **29,** 326–334 (2012).
32. Mason, T. G., Wilking, J. N., Meleson, K., Chang, C. B. & Graves, S. M. Nanoemulsions: Formation, structure, and physical properties. *J. Phys. Condens. Matter* **18,** R635–R666 (2006).
33. Solans, C. & Sole, I. Nano-emulsions: Formation by low-energy methods. *Curr. Opin. Colloid Interf.* **17,** 246–254 (2012).
34. Rosen, M. J. & Kunjappu, J. T. *Surfactants and Interfacial Phenomena* 4th edn (Wiley, 2012).
35. Matyjaszewski, K. & Davis, T. P. *Handbook of Radical Polymerization* 1st edn (Wiley, 2002).
36. Russev, S. C. & Arguirov, T. V. Rotating analyzer–fixed analyzer ellipsometer based on null type ellipsometer. *Rev. Sci. Instrum.* **70,** 3077–3082 (1999).

Acknowledgements

We acknowledge the contribution of S. C. Russev from Department of Solid State Physics & Microelectronics, Sofia University, Bulgaria, who helped us with the interpretation of the ellipsometric data and R. D. Stanimirova from Department of Chemical Engineering, Sofia University, Bulgaria, who performed measurements in a Langmuir trough and some spreading experiments. We also acknowledge R. K. Prud'homme from Department of Chemical and Biological Engineering (Princeton University) for the use of the Malvern Zetasizer. T.D.G. and S.D.S. acknowledge the financial support of EU project FP7-REGPOT-2011-1, 'Beyond Everest'. M.R. acknowledges D. Langevin for fruitful discussions. This research was made possible in part by the CMEDS grant from BP/The Gulf of Mexico Research Initiative.

Author contributions

J.F., M.R., L.N.A., S.D.S. and H.A.S. conceived of and planned the experiments. J.F. executed the experimental work. J.F., M.R. and H.A.S. wrote the manuscript. J.F. and D.V. analysed the DLS data. J.F., M.R., L.N.A., S.D.S., T.D.G. and H.A.S. analysed and interpreted the experimental results. T.D.G. and G.G.T. performed ellipsometry measurements. All authors reviewed the manuscript.

Additional information

Supplementary information is available in the online version of the paper. Reprints and permissions information is available online at www.nature.com/reprints. Correspondence and requests for materials should be addressed to J.F. or H.A.S.

Competing financial interests

The authors declare no competing financial interests.